https://doi.org/10.1007/s41230-025-4045-x

Evolution of microstructure and properties of Cu-12Fe alloys prepared by twin-roll strip casting

Tian-mo Wu, *Yuan-xiang Zhang, Shuai-jie Guo, Nuo-jin Wang, Jian Kang, and Guo Yuan
State Key Laboratory of Digital Steel, Northeastern University, Shenyang 110819, China

Abstract: The Cu-12Fe alloy has attracted significant attention due to its excellent electrical conductivity and electromagnetic shielding capability, high strength, cost-effectiveness, and recyclability. In the present work, the Cu-12Fe alloy strip with the thickness of 2.4 mm was successfully produced by twin-roll strip casting. The microstructure and properties of the Cu-12Fe alloy were tailored by cold rolling and aging treatment. The tensile strength of the as-cast strip is approximately 328 MPa and its elongation is 25%. The Fe phase randomly dispersed in the matrix, and the average size of Fe-rich phase is 2 μm. Besides, enrichment of Fe phase is observed in the central layer of the strip, results in the formation of the "sandwich structure". Moreover, the as-cast strip of Cu-12Fe was directly cold-rolled from 2.4 to 0.12 mm. The directly cold-rolled sample after aging at 450 °C for 16 h (Process I) shows excellent electrical conductivity of 69.5% IACS, the tensile strength and elongation are 513 MPa and 3.8%, the saturation magnetic flux density is 20.1 emu·g^{-1}, and the coercive force is 25.2 Oe. In Process II, the as-cast strip firstly cold-rolled to 1.2 mm, then aged at 500 °C for 1.5 h, followed by cold rolling to 0.12 mm, finally aged at 450 °C for 16 h. The sample after Process II shows the electrical conductivity of 66.3% IACS, the tensile strength of 533 MPa, an elongation of 3.5%, saturation magnetic flux density of 21.4 emu·g^{-1}, and the coercive force of 22.3 Oe.

Keywords: Cu-Fe alloy; twin-roll strip casting; microstructure; mechanical properties; thermal aging; electrical conductivity

CLC numbers: TG146.1$^+$1 **Document code:** A **Article ID:** 1672-6421(2026)01-073-10

1 Introduction

Cu-Fe alloys have attracted great attention due to their easy processability, low cost, excellent conductivity, and recyclability[1-2]. These alloys are widely applied in various industrial fields, such as aerospace, automotive connectors, mobile terminals, and medical devices like CT and MRI scanners, where they serve as essential shielding materials[3-5]. By precisely adjusting the fraction, size, and distribution of the α-Fe phase, Cu-Fe alloys can be granted exceptional mechanical properties, conductivity, and electromagnetic characteristics. The well-controlled Cu-Fe alloys exhibit superior electromagnetic wave shielding performance. Current advancements are focused on achieving a high content of uniformly distributed α-Fe phase to enhance the electrical and electromagnetic properties of Cu-Fe alloys. Further research and development efforts are crucial for refining the alloy microstructure to fulfill specific performance demands across a wide range of high-tech industries.

The Cu-Fe alloy system undergoes a transition to a metastable immiscible system when the concentration of dissolved Fe atoms in Cu exceeds 5%. In this condition, below the liquidus line, the alloy displays typical characteristics of a metastable immiscible system[6-7]. During solidification, a visible liquid phase separation and segregation occur that pose challenges in obtaining non-eutectic Fe phase particles with sizes less than or equal to 10 μm in the solidified structure. The limited solubility of Fe in Cu further complicates efforts to increase the proportion of a nanoscale Fe phase using conventional solidification processes and heat treatments. Alternative forming processes, such as mechanical alloying, micro/small melt pool construction (e.g., vacuum consumption and 3D printing), and microgravity solidification, have been

*Yuan-xiang Zhang
Ph. D., Associate Professor. His research interests mainly focus on the processes of sub-rapid solidification of special alloys in strip casting and related mechanisms.
E-mail: redyuanxiang@126.com
Received: 2024-03-11; Revised: 2024-05-22; Accepted: 2024-07-15

explored. However, these methods often come with high costs and deliver low efficiency, and are unsuitable in the case of thin strip materials[8]. There is an urgent necessity to develop more efficient and economical methods for producing Cu-Fe alloys with enhanced properties, particularly with respect to thin strip applications.

Several methods are currently employed to address the challenges associated with the Cu-Fe alloy system. The control of solidification behavior involves increasing the solidification cooling rate and adjusting the starting temperature in order to manage the separation process of metastable liquid phase. This approach aims to achieve the control over phase distribution during solidification. Microalloying and unconventional preparation methods involve modifying the morphology and proportion of primary Fe-rich phases, providing alternative approaches to influence the microstructure of alloys. The control of Fe atom solubility in the matrix represents an additional strategy. The solidification of Cu-Fe alloys results in a dual-phase microstructure, where the Fe phase is primarily distributed in the Cu matrix[9]. The amount of Fe-rich phases generated during solidification and the solute Fe atoms present in the matrix play a significant role in determining the ultimate mechanical and electromagnetic properties. Achieving a uniform distribution of Fe phases across micrometer to nanometer scales is crucial in enhancing the mechanical performance during subsequent deformation processing. The proposed strategies aim to optimize Cu-Fe alloy microstructure and properties, especially in applications that require thin strips.

This study adopts a strip twin-roll casting process with quasi-rapid solidification characteristics to prepare a Cu-12Fe alloy[10-12]. Twin-roll casting involves a continuous formation of liquid metal between rotating dual rolls, enabling high temperatures and rapid cooling of the liquid phase. The Cu-Fe alloy was solidified at a cooling rate of 1,000 °C·s^{-1} to inhibit metastable liquid-liquid phase separation, resulting in a uniform dispersion of nanoscale Fe phases. This process enhances the nucleation rate and shortens the growth cycle of primary Fe-rich phases, regulating the morphology and distribution of Fe phases in the alloy. An increase in the solubility of Fe atoms in the matrix results in an increased precipitation of nanoscale Fe phases.

A systematic characterization of the microstructure and assessment of the mechanical properties were conducted for Cu-12Fe alloy strips prepared by twin-roll casting. The influence of different cold rolling stages and heat treatment on the microstructure, mechanical properties, and electrical conductivity of the alloy was also studied. In addition, the underlying mechanisms associated with the observed effects were addressed.

2 Materials and methods

This work employed a twin-roll strip casting device for the preparation of the Cu-12Fe alloy. Pure Cu (99.8%) and Fe (electrolytic iron with a purity of 99.97%) were used as raw materials. Samples were melted under vacuum (5–12 Pa) in a high-purity graphite crucible using an induction furnace. The relevant parameters of the casting and rolling process are shown in Table 1. The casting roll was made of water-cooled beryllium copper with chromium plating, and the plating thickness is 50 μm. The final product was a thin Cu-12Fe alloy strip with a width of 110 mm and thickness of 2.4 mm. The measured alloy composition was 88.2wt.% Cu and 11.8wt.% Fe.

Table 1: Cast-rolling parameters

Parameters	Unit	Values
Width of the casting rolls	mm	110
Casting roller diameter	mm	500
Casting temperature	°C	Approximately 1,450
Cast rolling force	kN	10±2
Cooling water flux	$m^3 \cdot h^{-1}$	30
Cast rolling speed	$m \cdot min^{-1}$	35
Molten pool height	mm	150±10

The alloy forming process is illustrated in Fig. 1(a). Two distinct forming processes were implemented. Process I involved cold rolling followed by aging treatment at 450 °C for durations of 1, 2, 4, 8, and 16 h, respectively. Process II consisted of cold rolling, then a heat treatment at 500 °C for 90 min, and subsequently an aging treatment at 450 °C for the same durations of 1, 2, 4, 8, and 16 h, respectively. The alloy strip, as shown in Fig. 1(b), was directly cold-rolled from a thickness of 2.4 mm to 0.12 mm. Table 2 provides the cold rolling process parameters. The subsequent solidified strip structure was assessed using an OLYMPUS-BX53M metallographic microscope. Electron backscatter diffraction (EBSD) was conducted on a scanning electron microscope (Symmetry, Oxford Instruments); and Channel 5 software was used for EBSD data analysis. X-ray diffraction (XRD) phase analysis was performed using a Smartlab 9 kW X-ray diffractometer. Electrical conductivity was measured using the double-arm bridge method that is commonly applied for testing the conductivity of metal foils with low resistance. Mechanical properties of the alloy were tested at room temperature using a 100 kN electronic universal testing machine (Taiwan High Speed) with dog-bone-shaped tensile samples with a gauge length of 10 mm and a cross-sectional size of 0.12 mm×5 mm. Fracture surface morphology images were captured using a ZEISS Ultra55 scanning electron microscope (SEM). The magnetic properties of the samples were assessed using a Lakeshore-7400s vibrating sample magnetometer (VSM). Focused ion beam (FIB, ZEISS) combined with transmission electron microscopy (TEM, JEM-2100) analysis was also employed to determine alloy's microstructure.

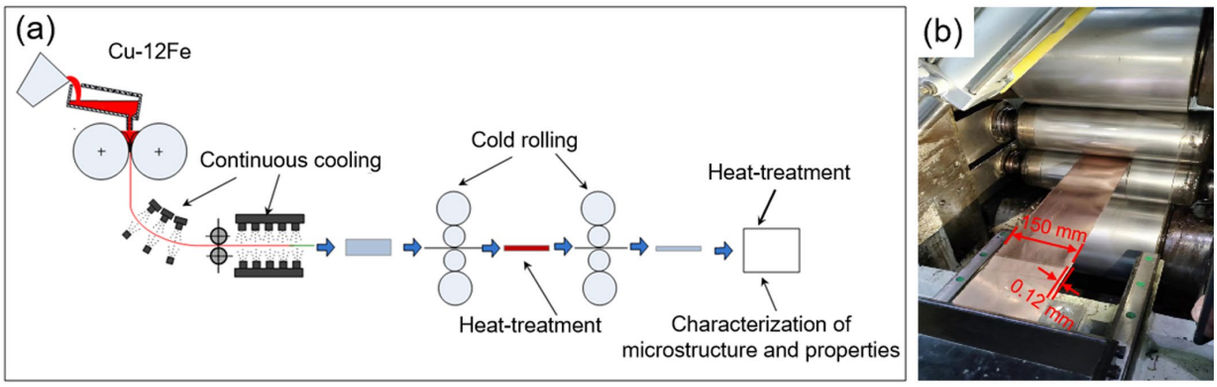

Fig. 1: Schematic representation of the experimental Cu-12Fe alloy forming procedure (a) and cold rolling process (b)

Table 2: Cold rolling process parameters

Parameters	Unit	Values
Cold rolling speed	$m \cdot s^{-1}$	0.03
Rolling force	kN	50–250
Roll diameter	mm	150
Rolling reduction per pass	mm	0.05–0.2

3 Results and discussion

Figure 2 shows the phase diagram of Cu-Fe binary alloy calculated using Thermo Calc software. The Cu-Fe binary alloy system exhibits a metastable miscibility gap, which has been confirmed both thermodynamically and through experimental means. This miscibility gap is represented by the blue dashed line in Fig. 2. Undercooling the alloy to the metastable miscibility gap triggers liquid-liquid phase separation, resulting in the formation of two distinct liquid phases that are immiscible. The occurrence of metastable liquid-liquid phase separation in specific alloy compositions primarily depends on the extent of undercooling.

In this study, the critical undercooling (ΔT_c) is defined as the difference between the liquidus and the miscibility gap line. If the actual undercooling (ΔT) of the Cu-Fe alloy melt is below ΔT_c, the undercooled liquid phase will fail to infiltrate the immiscible region of the metastable liquid phase components, resulting in the occurrence of a liquid-solid phase transition. Conversely, when the actual undercooling (ΔT) exceeds ΔT_c, the undercooled alloy melt enters the immiscible region, initiating a liquid-liquid phase separation transition during subsequent solidification.

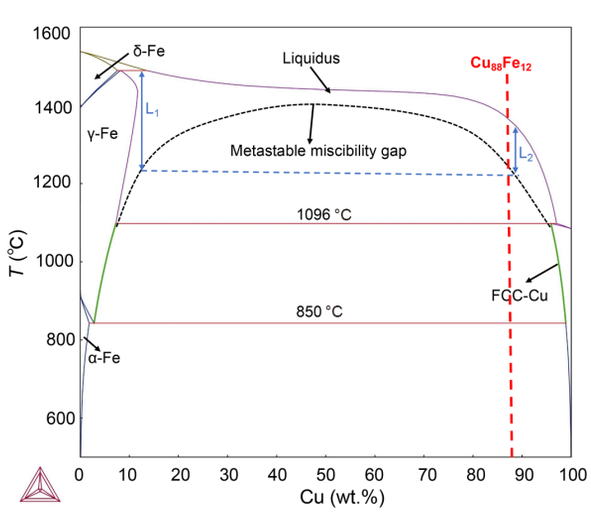

Fig. 2: Cu-Fe alloy phase diagram

During the solidification process, nucleation of a trace minute amount of Fe-rich phase generates spherical droplets. These droplets undergo diffusion-driven growth, accompanied by coarsening through various mechanisms, and exhibit Marangoni migration influenced by interfacial energy gradients, as well as Stokes motion induced by gravity[13]. The movement of these Fe-rich liquid droplets involves collision, aggregation, and coalescence that is subject to Oswald ripening and Brownian motion[14]. The vertical dashed red line on the right-hand side of Fig. 2 delineates the solidification process for a Cu-Fe alloy with a 12wt.% Fe content, illustrating the constitution of FCC-Cu and BCC-Fe phases.

The metallographic microstructure of the target alloy strip is illustrated in Fig. 3. It can be seen that the Fe phase in the Cu-12Fe alloy, produced by the twin-roll thin strip casting and rolling process, appears spherical rather than dendritic. Moreover, the Fe particles are not fused together but are clearly separated. The morphology of the Fe phase differs significantly from that reported for other preparation methods[15-16]. Liu et al.[9] have investigated the influence of cooling rate on the grain morphology of the Cu-Fe alloy, demonstrating a transition from dendritic to spherical grains, with the majority of the Fe phases exhibiting equiaxed grains at cooling rates above 560 $K \cdot s^{-1}$. The Fe phase demonstrates a central enrichment, which attributes to the Marangoni migration effect during solidification. The centrally enriched Fe phase, with the Cu matrix on both sides, forms a sandwich-like structure, which can effectively enhance the electromagnetic shielding effect of the Cu-Fe alloy.

The EBSD analysis of the Cu-12Fe alloy strip is presented in Fig. 4. In the inverse pole figure (IPF) map in Fig. 4(a), the gray and black lines are used to denote the low-angle grain boundaries (with orientation deviations within 2°–15°) and high-angle grain boundaries (with orientation deviations exceeding 15°), respectively. It can be seen that the low-angle

grain boundary component is significantly lower, consistent with the characteristics of recrystallization in Cu-Fe alloys [17].

The distribution of the Fe phase in the alloy is shown in Fig. 4(b), where the gray area represents the Cu matrix, and the average grain size of the spherical Fe phase is about 2 μm. In addition, the crystal orientation distribution of Cu and Fe phases in the alloy is presented as {100}, {110}, and {111} pole figures in Fig. 4(c). The orientation of the alloy strip is relatively scattered, and the texture intensity is low, with a maximum texture intensity for Cu and Fe phases of 1.64 and 2.13, respectively.

The tensile data and fracture morphology of the cast strip are shown in Fig. 5. An alloy strip strength of 328 MPa is observed from the stress vs. strain curve in Fig. 5(a), with an associated elongation of 25% that represents good ductility. The fracture morphology of the strip is illustrated in the images presented in Figs. 5(b) and (c). The presence of numerous dimples on the fracture surface is indicative of a ductile fracture mode. The dimples are small, clustered, and not well dispersed. It can be observed that the Fe phase particles are separated from each other. Some dimples contain Fe particles, as indicated by the blue circle in Fig. 5(c), while others do not, as represented by the green circle. The distribution of the spherical Fe phase particles does not affect the subsequent rolling and strip formation. This also suggests that the fracture mode of the Cu-12Fe alloy strip is ductile. The separation of the Fe phases in the alloy minimizes the possibility of cracking during rolling. The matrix of the cast strip exhibits an elongation of 25%, indicating enhanced ductility that facilitates a direct cold rolling to a thickness of 0.12 mm in a single stage.

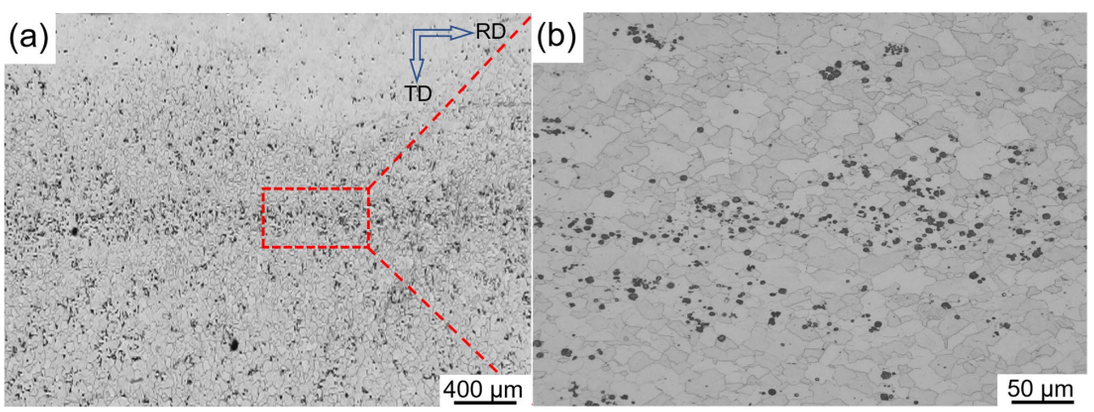

Fig. 3: Microstructure of Cu-12Fe alloy strip (a) and the enlarged figure of the region marked in (a) (b)

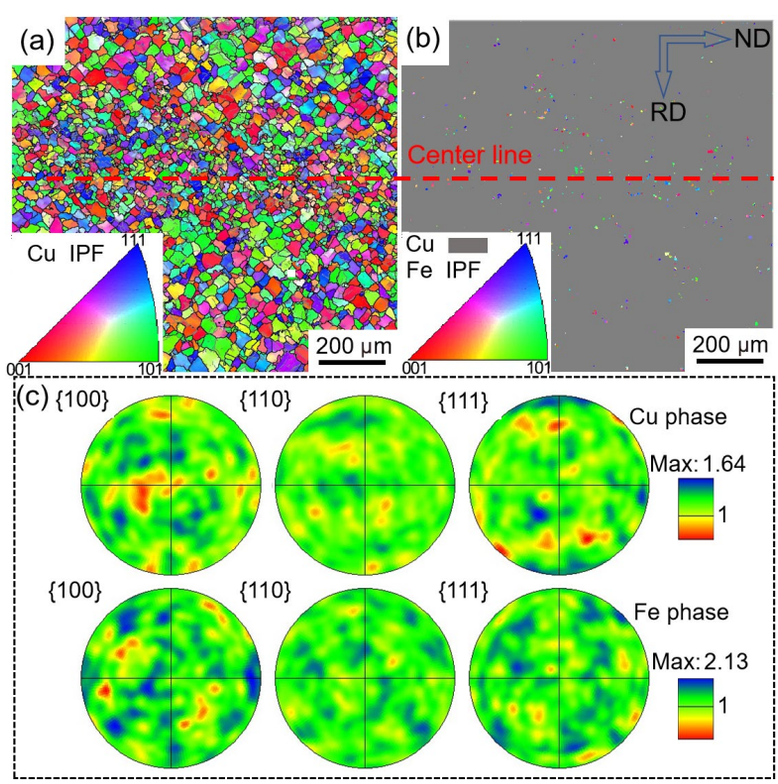

Fig. 4: Microstructure of Cu-12Fe alloy strip: (a) inverse pole figures (IPF) showing the orientation of each grain; (b) Fe phase distribution corresponding to Fig. 3(a); (c) {100}, {110}, and {111} pole figures for the Cu (upper row) and Fe (lower row) phases

The EBSD data generated for the alloy subjected to Processes I and II after aging at 450 °C for 16 h are presented in Fig. 6. There is no significant difference in the texture distribution following Process I [Fig. 6(b)] or Process II [Fig. 6(e)]. However, from a consideration of Figs. 6(c) and (f), it is evident that after rolling, the texture strength of the cast strip is significantly increased. The prominent texture spots may be observed in the orientation distribution function (ODF) maps at φ_2=45°. Following the Process I and Process II, the main texture spots are {112}<1-10>, {110}<1-11>, and {223}<1-10>, as shown in Figs. 6(b) and (e). In terms of face texture, the principal alloy orientations are the [111] and [110] planes.

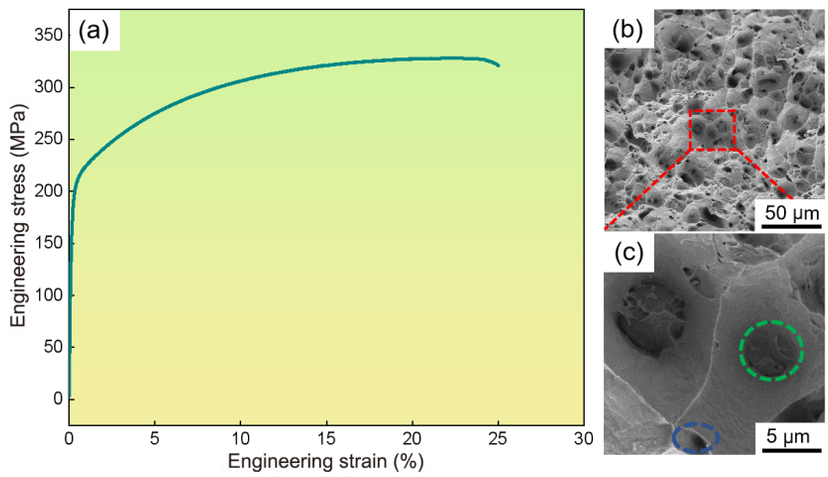

Fig. 5: Stress-strain curve of Cu-12Fe alloy strip (a), surface fracture morphology (b), and a magnified image of the area identified by the red dashed rectangle in (b) (c)

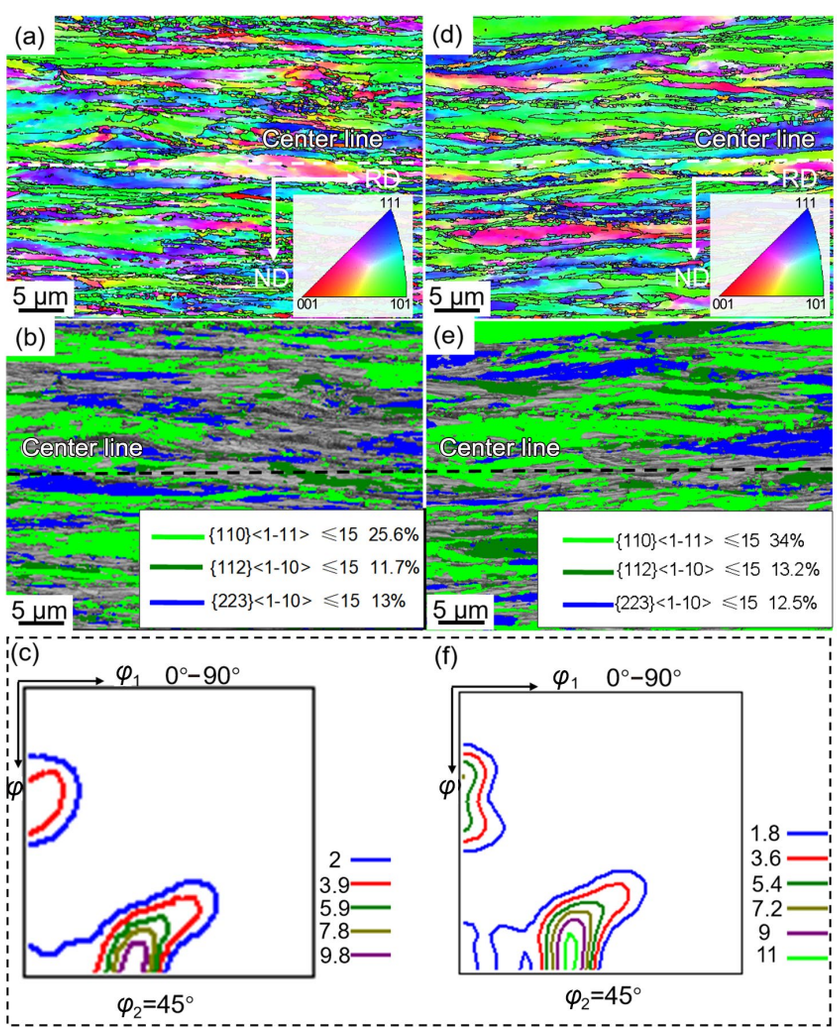

Fig. 6: EBSD analysis of the Cu-12Fe alloy after two processes (aged at 450 °C for 16 h): (a) and (d) IPF maps; (b) and (e) texture maps; (c) and (f) orientation distribution function maps at φ_2 = 45°

The impact of aging duration on mechanical properties of the alloys is shown in Fig. 7. The strength of the alloy significantly increases after cold rolling compared to the as-cast strip in Fig. 5. As shown in Fig. 7(a), both Process I and Process II alloys exhibit an increasing trend in tensile strength with increasing aging time. Conversely, hardness of the alloys decreases markedly with increasing aging time [Fig. 7(b)] before attaining a stable value (at times exceeding 4 h). The measured hardness reaches 134.6 HV and 132.6 HV for the Process I and Process II, respectively, after aging at 450 °C for 16 h. The observed decrease in hardness can be attributed to an annealing during heat treatment that serves to counteract the work-hardening effect generated during cold rolling[18].

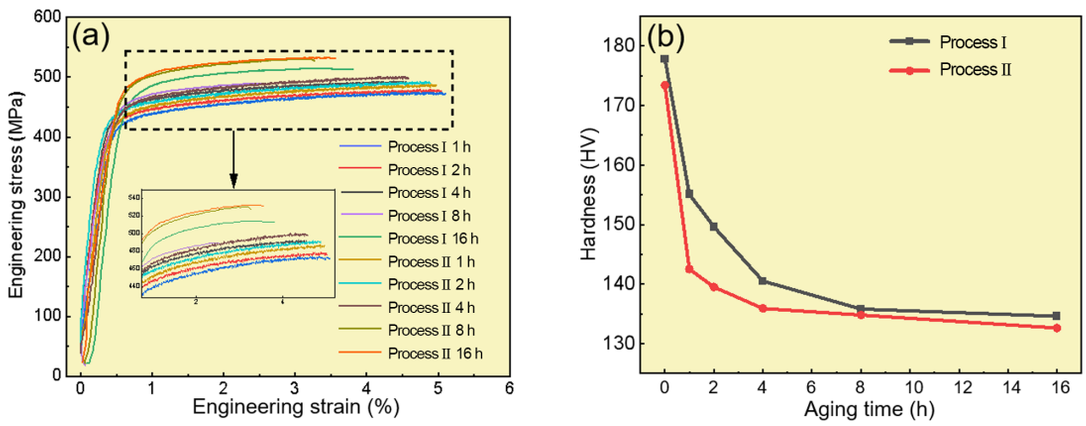

Fig. 7: Mechanical properties of the Cu-12Fe alloy after aging at 450 °C for different durations: (a) strength; (b) hardness

The primary strengthening mechanism considered in this study is precipitation strengthening and grain/substructure boundary strengthening. The Process II samples (aged for 16 h) were selected for analyzing the strengthening mechanism. The Orowan mechanism is a typical strengthening mechanism that applies to precipitation-hardened Cu alloys[19-20]. In the Cu matrix, nanoscale Fe precipitates interact with dislocations to enhance the strength of the alloy. The strengthening mechanism of dislocations bypassing non-deformable particles can be expressed by the Orowan-Ashby equation[21]:

$$\Delta\sigma_{\text{Orowan}} = 0.81 \cdot \frac{MGb}{(1-\nu)^{\frac{1}{2}}} \cdot \frac{\ln(\frac{d_{\text{precip}}}{b})}{d_{\text{precip}} \cdot \sqrt{\frac{3\pi}{2f_{\text{precip}}}} - d_{\text{precip}}} \quad (1)$$

where M represents the Taylor factor (3.08[22]), G is the shear modulus of the Cu matrix (48 GPa[23]), b denotes the Burgers vector (0.255 nm[24]), ν is Poisson's ratio (0.34[25]), d_{precip} represents the average size of the precipitated crystal grains, and f_{precip} is the precipitation volume fraction. The Orowan-Ashby equation suggests that the strengthening effect is more pronounced for smaller precipitates. In addition, when the precipitate size is relatively constant, a higher volume fraction contributes to a more effective strengthening effect. In the case of the alloy under consideration, the analysis has focused on smaller secondary precipitates of the order of tens of nanometers, as opposed to larger particle precipitates or atomic-scale precipitates. The calculated yield increment for the Process I is about 112 MPa (d_{precip}=23.3 nm, f_{precip}=0.95%), which is lower than the value of about 116 MPa (d_{precip}=23.1 nm, f_{precip}=1.01%) for the Process II.

The grain size also plays an important role in strengthening metallic materials. The Hall-Petch Eq. (2) is commonly used to calculate the incremental strength[26]:

$$\Delta\sigma_{\text{gs}} = \frac{\kappa}{\sqrt{d_{\text{grain}}}} \quad (2)$$

where κ is a constant for the copper alloy (=0.14[27]), and d_{grain} represents the average grain diameter. The calculated yield increment for the Process I is 297.8 MPa (d_{grain}=0.221 μm), significantly higher than that calculated for the Process II of 312.3 MPa (d_{grain}=0.201 μm).

The total strength can be obtained from:

$$\sigma_{\text{total}} = \sigma_0 + \Delta\sigma_{\text{Orowan}} + \Delta\sigma_{\text{gs}} \quad (3)$$

where σ_0 is the inherent lattice strength of the copper alloy, which is estimated to equal 50 MPa[28]. The calculated yield strength for the Process I is 459.8 MPa, which shows a deviation from the experimental result (479.0 MPa). In the case of the Process II, the calculated yield strength is 478.3 MPa, which also deviates from the measured value (496.5 MPa). The observed difference in experimental and calculated values may be attributed to work hardening and the presence of some large precipitates.

The X-ray diffraction (XRD) patterns shown in Fig. 8(a) demonstrate that the Cu-12Fe alloy consists of FCC-Cu phase and α-Fe phase, where differences in the cold rolling process and aging treatment do not affect the crystal structure. Although the phase constitution of the alloy remains unchanged after aging, the diffraction peaks for α-Fe and Cu in the alloy thin strip post-treatment are shifted slightly to the right compared to the as-cast sample [Fig. 8(b)]. This suggests a reduction in the alloy lattice parameters and a precipitation of solute Fe atoms from the matrix. The results indicate that aging promotes precipitation of the Fe phase in the Cu-12Fe alloy.

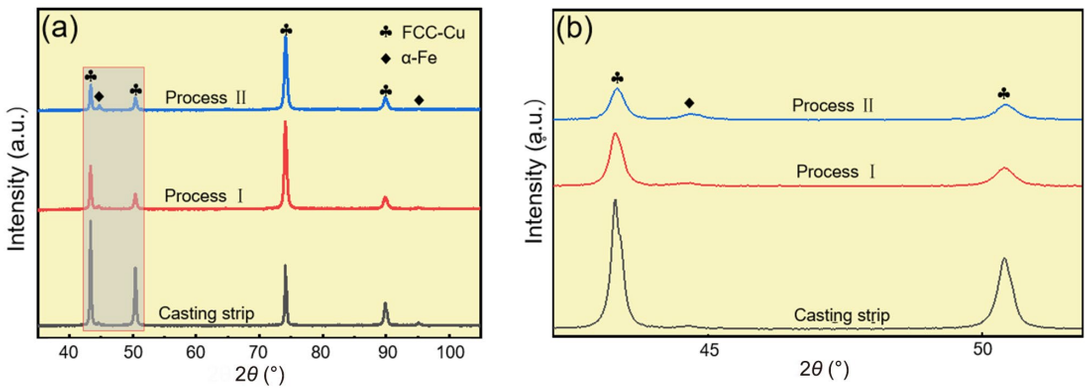

Fig. 8: X-ray diffraction patterns for the Cu-12Fe alloy samples (a) and an expanded pattern for the region highlighted in grey region in (a) (b)

The results of a systematic sample characterization by FIB/TEM are presented in Fig. 9. A large number of uniformly dispersed nanoscale particles were detected [Figs. 9(a) and (b)], where statistical analysis reveals an average size of larger precipitates of about 100 nm. Smaller precipitates are also observed, as shown in Fig. 9(c). Based on the HRTEM analysis presented in Figs. 9(d) and (e), the nanoscale particles are identified as BCC-Fe, which exhibits a clear crystallographic orientation relationship with the Cu matrix [$(1\text{-}11)_{Cu}$// $(1\text{-}10)_{Fe}$].

The analysis has revealed a hierarchical precipitation of Fe particles in the Cu-12Fe alloy. This precipitation behavior can be divided into three stages. Firstly, during high-temperature solidification, Fe precipitates from the liquid phase, aggregates and grows into larger Fe particles, as shown in the green and orange encircled particles in Figs. 9(a) and (b). The particle identified by the green circle represents a primary precipitated

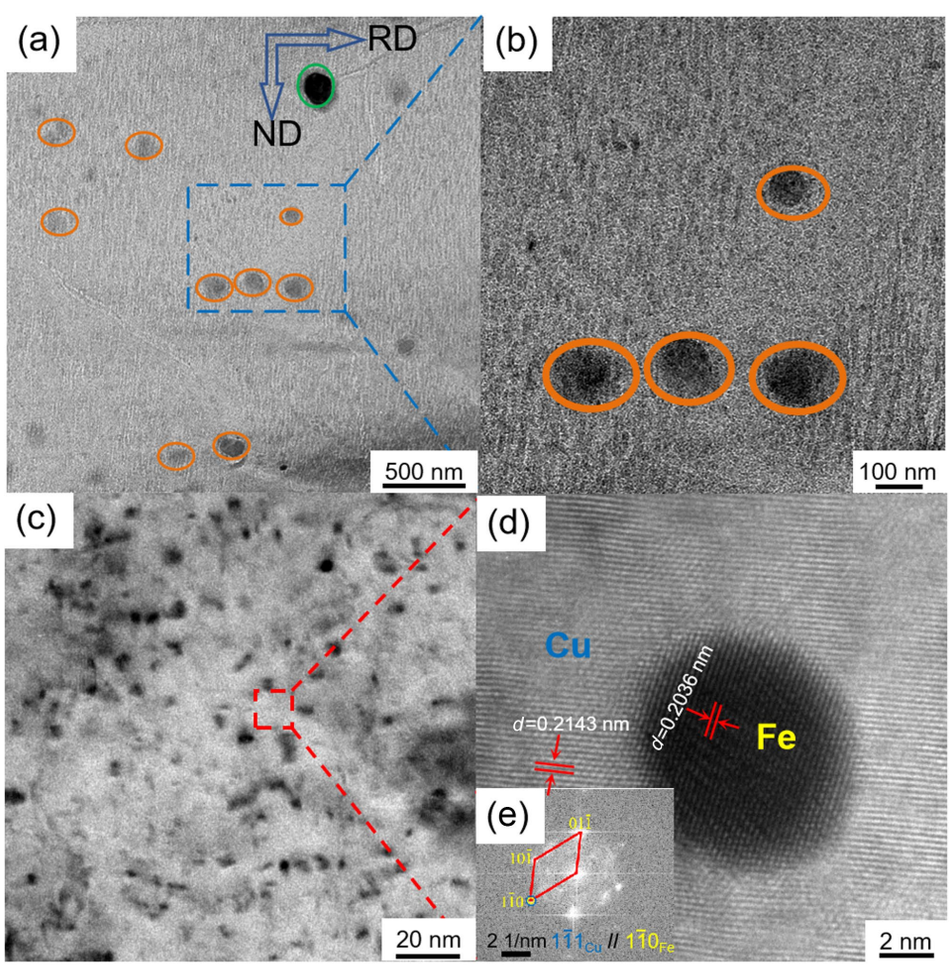

Fig. 9: TEM analysis of Cu-12Fe alloy subjected to Process II and thermal aging at 450 °C for 16 h; (a) and (b) distribution of Fe phase particles in the Cu-12Fe alloy; (c) higher magnification image showing the distribution of the nano-sized precipitated Fe phase in the alloy; (d) enlarged image of area identified by the red square in (c); (e) FFT of (d)

large Fe particle, whereas the orange circles identify finer Fe particles that continue to precipitate during the cooling process. Secondly, Fe precipitates following solidification in the form of submicron-sized particles, which then undergo aging and cooling, resulting in the formation of Fe particles with sizes ranging from several nanometers to tens of nanometers, as shown in Fig. 9(c). Thirdly, stage involves the precipitation of nanoscale Fe particles during the aging process of the rolled deformable matrix. At this point, the precipitated Fe particles are well dispersed, with some approaching atomic-level sizes.

The FIB/TEM analysis demonstrates that a substantial number of nanoscale α-Fe particles precipitated from the Cu-rich matrix following prolonged thermal aging. This phenomenon may be associated with the relatively high Fe content in the Cu-12Fe alloy and the limited solubility of Fe atoms in the Cu matrix, which results in the presence of excess Fe particles in the form of precipitated second-phase particles.

The variation in the electrical conductivity of the alloy with aging time of 0 to 16 h at 450 °C is shown in Fig. 10. A marked increase in electrical conductivity is observed in the first hour followed by a gradual increase with extended thermal treatment to reach values of 69.5% IACS and 66.3% IACS after 16 h for both the Process I and Process II, respectively. During the heat treatment, Fe atoms precipitate from the Cu matrix. As the electrical conductivity of the Cu-Fe alloy is dependent on the electron scattering effect of solute atoms in the matrix, an increased conductivity results from the precipitation of solute atoms. Electrical resistance in the alloy originates from the scattering of solute atoms, presence of vacancy, and point defects in the matrix. During aging, precipitation of solute atoms and a dislocation short-circuit diffusion contribute to higher conductivity[29]. The solute atoms can be transferred from the copper matrix to precipitate where the dislocation network acts as nucleation sites for the precipitation process[30].

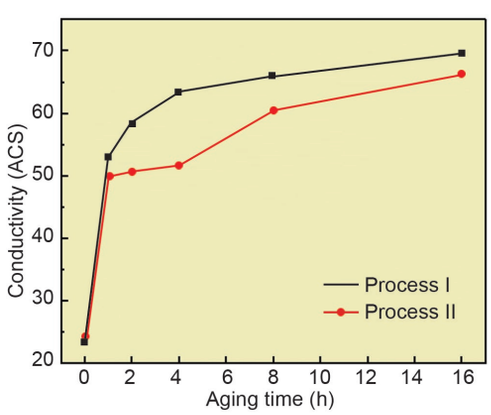

Fig. 10: Variation in alloy electrical conductivity as a function of aging time at 450 °C in Process I and Process II

The relationship between the relevant diffusion coefficients is given by:

$$D_0 = D_L(1-f) + D_P f \quad (4)$$

where D_0 represents the diffusion coefficient, D_L is the diffusion coefficient of the lattice, f is the fraction of diffusion atoms in the dislocation, and D_P is the diffusion coefficient in the dislocation.

The Eq. (4) can also be expressed as:

$$D_0 = D_L + D_P A_P(\rho + \Delta\rho) \quad (5)$$

where the A_P is the area, $\rho+\Delta\rho$ is the dislocation density, and $\Delta\rho$ is the increase of dislocation density by the pre-existing precipitates.

The diffusion coefficient of atoms at the dislocation core is much greater than the diffusion coefficient of atoms between lattice planes[31]. Following cold rolling, the alloy experiences a significant increase in dislocation density. Solutes can travel to form precipitates, facilitated by the channels associated with dislocations formed in the aging process. From Eq. (5), it can be observed that, with A_P remaining constant and D_L being a constant value, the diffusion coefficient D_0 increases with an increase in dislocation density (i.e., an increase in $\rho+\Delta\rho$), allowing more solute atoms to diffuse within the alloy. Consequently, the Cu matrix is purified during the aging process, leading to a decrease in resistance. Simultaneously, the significant precipitation of solute atoms during aging reduces their electron scattering effect. Overall, the improvement in alloy conductivity mainly depends on the reduction of the electron scattering effect of solute atoms and the increase in the diffusion coefficient.

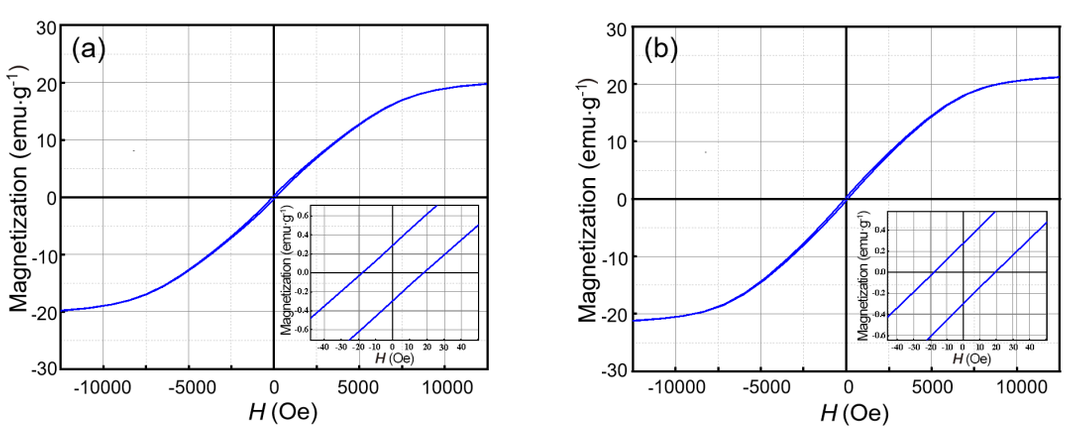

Fig. 11: Magnetic properties of the Cu-12Fe alloy: (a) hysteresis loop associated with the Process I; (b) hysteresis loop associated with the Process II

Copper-iron (Cu-Fe) alloys, as soft magnetic materials, have significant potential in a range of applications. An analysis of the magnetic properties of samples subjected to aging at 450 °C for 16 h was conducted; and the magnetic hysteresis loops for the Process I and Process II are presented in Fig. 11. It can be seen that the alloys exhibit soft magnetic behavior, characterized by narrow hysteresis loops. The results indicate that variations in the cold rolling process have little effect on the resultant saturation magnetization (Ms) and coercivity (Hc). The saturation magnetization for the Process I alloy is 20.1 emu·g^{-1}, with a coercivity of 25.2 Oe. In the case of the Process II, the saturation magnetization is 21.4 emu·g^{-1}, with a coercivity of 22.3 Oe.

Figure 12 shows the strength and electrical conductivity of the Cu-Fe alloys in this study and those values reported in literature[32–37]. It is evident that the alloys prepared using the twin-roll strip casting process in this study, followed by cold rolling and aging treatment, achieve a good balance between electrical conductivity and strength, with a significantly higher electrical conductivity than those in literature.

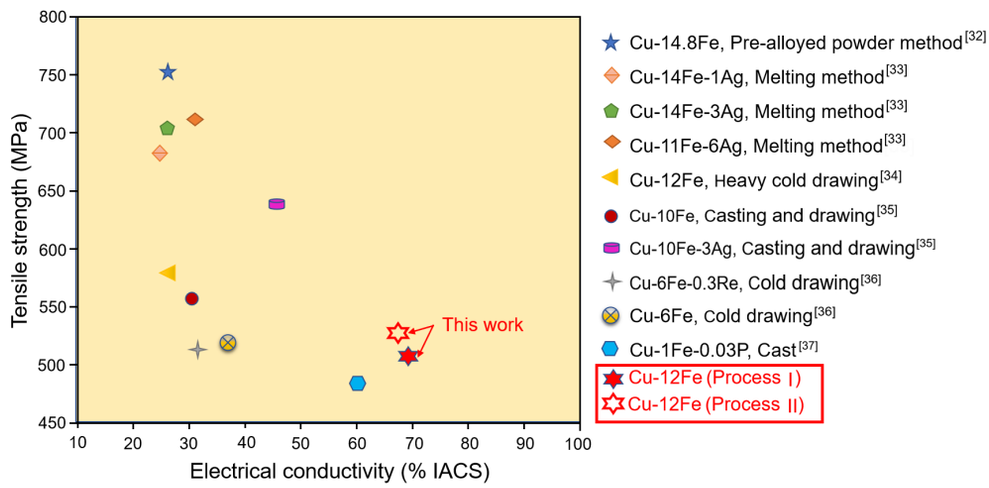

Fig. 12: Comparison of strength and electrical conductivity of the Cu-Fe alloys in this study and those reported in literature[32–37]

4 Conclusions

(1) The twin-roll casting technology provides a novel route to efficiently produce the Cu-12Fe alloy. The sub-rapid solidification, occurring at a rate of approximately 1,000 °C·s^{-1}, effectively inhibits metastable liquid phase separation between Cu and Fe. The size of primary Fe phase ranges from 1 to 8 μm, and the average grain size is 2 μm. Therefore, the growth and coalescence of Fe phase are effectively inhibited during the sub-rapid solidification.

(2) In the as-cast strip, the Fe phase is enriched in the central layer and randomly dispersed in the matrix, generating a "sandwich-like" structure composed of Cu-Fe-Cu. The specific structure is conductive to the improvement of electromagnetic shielding. Besides, the as-cast strip shows superior plasticity with an elongation of 25%, which can be directly cold-rolled from 2.4 to 0.12 mm.

(3) The as-cast strip subjected to cold-rolling and aging process exhibits excellent properties. In Process I (aging at 450 °C for 16 h), the tensile strength is 513 MPa and the electrical conductivity is 69.5% IACS, the saturation magnetization is 20.1 emu·g^{-1} and coercivity is 25.2 Oe. In Process II (aging at 450 °C for 16 h), the tensile strength is 533 MPa and the electrical conductivity is 66.3% IACS, the saturation magnetization is 21.4 emu·g^{-1} and coercivity is 22.3 Oe.

(4) The micro-sized and numerous nano-sized Fe phases can be observed in the aged samples, indicating a three-stage precipitation pattern of the Fe phase in Cu-Fe alloy. Firstly, the micro-sized Fe phase is precipitated during the final solidification stage. Then, after the solidification process completed, the remained high temperature also facilitates the precipitation of Fe phase. Finally, the nano-sized Fe phase precipitates during aging process. The precipitation of numerous nano-sized Fe phase can not only enhance the strength, but also reduce electron scattering and improve the electrical conductivity of the Cu-12Fe alloy.

Acknowledgments

This work was financially supported by the Natural Science Foundation of Liaoning Province of China (2022-MS-109), the Key Research and Development Program of Liaoning Province (2023JH2/101800045), and the Ministry of Science and Technology of the Peoples Republic of China (ZZ2021006).

Conflict of interest

The authors declare that they have no known competing financial interests or personal relationships that could have appeared to influence the work reported in this paper.

References

[1] Pingale A D, Owhal A, Katarkar A S, et al. Recent researches on Cu-Ni alloy matrix composites through electrodeposition and powder metallurgy methods: A review. Mater's Today Proc., 2021, 47: 3301–3308.

[2] Tian Y Z, Yang Y, Peng S Y, et al. Managing mechanical and electrical properties of nanostructured Cu-Fe composite by aging treatment. Mater. Char., 2023, 196: 112600.
[3] Wang M, Jiang Y, Li Z, et al. Microstructure evolution and deformation behaviour of Cu-10 wt%Fe alloy during cold rolling. Mater. Sci. Eng. A, 2021, 801: 140379.
[4] Li J, Ding H, Li B, et al. Microstructure evolution and properties of a Cu-Cr-Zr alloy with high strength and high conductivity. Mater. Sci. Eng. A, 2021, 819: 141464.
[5] Li R. Zhang S, Zou C, et al. The roles of Hf element in optimizing strength, ductility and electrical conductivity of copper alloys. Mater. Sci. Eng. A, 2019, 758: 130–138.
[6] He J, Zhao J Z, Ratke L. Solidification microstructure and dynamics of metastable phase transformation in undercooled liquid Cu-Fe alloys. Acta Mater., 2006, 54(7): 1749–1757.
[7] Wilde G, Perepezko J H. Critical-point wetting at the metastable chemical binodal in undercooled Fe-Cu alloys. Acta Mater., 1999, 47(10): 3009–3021.
[8] Zuo X W, Wang E G, Han H, et al. Magnetic properties of Fe-49%Sn monotectic alloys solidified under a high magnetic field. Journal of Alloys and Compounds, 2010, 492(1–2): 621–624, https://doi.org/10.1016/j.jallcom.2009.11.195.
[9] Liu S, Jie J, Guo Z, et al. Solidification microstructure evolution and its corresponding mechanism of metastable immiscible Cu80Fe20 alloy with different cooling conditions. J. Alloys Compd., 2018, 742: 99–106.
[10] Xia Y, Zhang Y, Wu T, et al. Deformation twinning caused by warm rolling and secondary recrystallization in twin-roll strip casting Fe81Ga19 alloy. J. Alloys Compd., 2022, 922: 166039.
[11] Zhang C, Yuan G, Zhang Y, et al. Cu-based amorphous alloy plates fabricated via twin-roll strip casting. Mater. Sci. Eng. A, 2021, 828: 142123.
[12] Lu X, Fang F, Zhang Y, et al. Evolution of microstructure and texture in grain-oriented 6.5%Si steel processed by strip-casting. Mater. Charact., 2017, 126: 125–134.
[13] Zhao J, Zhang L, Li Z, et al. Topological structure evolvement of flow and temperature fields in deformable drop Marangoni migration in microgravity. Int. J. Heat Mass. Tran., 2011, 54: 4655–4663.
[14] Shi R, Wang Y, Wang C, et al. Self-organization of core-shell and core-shell-corona structures in small liquid droplets. Appl. Phys. Lett., 2011, 98: 204106.
[15] Liu S, Jie J, Guo Z, et al. A comprehensive investigation on microstructure and magnetic properties of immiscible Cu-Fe alloys with variation of Fe content. Mater. Chem. Phys., 2022, 921: 166163.
[16] Yue S, Li G, Qu J, et al. Investigation on the dual-phase co-deformation behavior and strengthening mechanism in cold-drawn Cu-20Fe alloy. Mater. Sci. Eng. A, 2023, 862: 144474.
[17] Wang M, Jiang Y, Li Z, et al. Microstructure evolution and deformation behaviour of Cu-10wt%Fe alloy during cold rolling. Mater. Sci. Eng. A, 2021, 801: 140379.
[18] Yamashita T, Koga N, Kawasaki T, et al. Work hardening behavior of dual phase copper-iron alloy at low temperature. Mater. Sci. Eng. A, 2021, 819: 141509.
[19] Schwich H, Gorzen D, Blinn B, et al. Characterization of the precipitation behavior and resulting mechanical properties of copper-alloyed ferritic steel. Mater. Sci. Eng. A, 2020, 772: 138807.
[20] Chatterjee A, Sprague E, Mazumder J, et al. Hierarchical microstructures and deformation behavior of laser direct-metal-deposited Cu-Fe alloys. Mater. Sci. Eng. A, 2021, 802: 140659.
[21] Peng H, Xie W, Chen H, et al. Effect of micro-alloying element Ti on mechanical properties of Cu-Cr alloy. J. Alloys Compd., 2021, 852: 157004.
[22] Wang X, Xiao Z, Qiu W, et al. The evolution of microstructure and properties of a Cu-Ti-Cr-Mg-Si alloy with high strength during the multi-stage thermomechanical treatment. Mater. Sci. Eng. A, 2021, 803: 140510.
[23] Huang J, Xiao Z, Dai J, et al. Microstructure and properties of a novel Cu-Ni-Co-Si-Mg alloy with super-high strength and conductivity. Mater. Sci. Eng. A, 2019, 744: 754–763.
[24] Chen J, Wang J, Xiao X, et al. Contribution of Zr to strength and grain refinement in Cu-Cr-Zr alloy. Mater. Sci. Eng. A, 2019, 756: 464–473.
[25] Yu J, Zhou D, Pu C, et al. Prediction of stable Cu-Li binary intermetallics from first-principles calculations: Stoichiometries, crystal structures, and physical properties. J. Alloys Compd., 2018, 766: 640–648.
[26] Wang W, Zhu J, Qin N, et al. Effects of minor rare earths on the microstructure and properties of Cu-Cr-Zr alloy. J. Alloys Compd., 2020, 847: 155762.
[27] Zhu X, Xiao Z, An J, et al. Microstructure and properties of Cu-Ag alloy prepared by continuously directional solidification. J. Alloys Compd., 2021, 883: 160769.
[28] Biselli C, Morris D. Microstructure and strength of Cu-Fe in situ composites after very high drawing strains. Acta Mater., 1996, 44(2): 493–504.
[29] Humphreys F, Hirsch P. The deformation of single crystals of copper and copper-zinc alloys containing alumina particles. I. Macroscopic properties and work-hardening theory. In: Proceedings of the Royal Society: A, 1970, 318: 73–90.
[30] Zhang D, Zhao D, Dong Q, et al. Effect of complex-aging in Cu-Ni-Si alloy. Funct. Mater., 2004, 35: 2160–2163.
[31] Har E W. On the role of dislocations in bulk diffusion. Acta Metall., 1957, 5: 597–612.
[32] Wang F, Wakoh K, Li Y, et al. Study of microstructure evolution and properties of Cu-Fe microcomposites produced by a pre-alloyed powder method. Mater. Des., 2017, 126: 64–72.
[33] Gao H, Wang J, Shu D, et al. Effect of Ag on the microstructure and properties of Cu-Fe in situ composites. Scr. Mater., 2005, 53(10): 1105–1109.
[34] Wu Z, Liu J, Chen Y, et al. Microstructure, mechanical properties and electrical conductivity of Cu-12wt.% Fe microcomposite annealed at different temperatures. J. Alloys Compd., 2009, 467(1–2): 213–218.
[35] Li Y, Yi D, Zhang J. Comparative study of the influence of Ag on the microstructure and mechanical properties of Cu-10Fe in situ composites. J. Alloys Compd., 2015, 647: 413–418.
[36] Wu Z, Zhang J, Chen Y, et al. Effect of rare earth addition on microstructural, mechanical and electrical characteristics of Cu-6% Fe microcomposites. J. Rare Earths, 2009, 27(1): 87–91.
[37] Lu D, Wang J, Zeng W, et al. Study on high-strength and high-conductivity Cu-Fe-P alloys. Mater. Sci. Eng. A, 2006, 421(1–2): 254–259.